

1 Nanoscale Buckling in Lamellar Block Polymers: A Molecular 2 Dynamics Simulation Approach

3 Ali Makke,^{†,‡,||} Olivier Lame,[‡] Michel Perez,[‡] and Jean-Louis Barrat^{*,§}

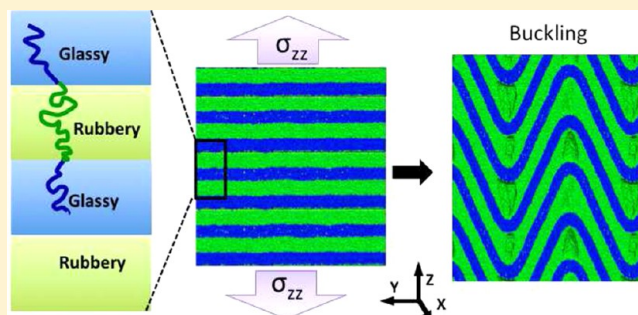
4 [†]LPMCN, UMR CNRS 5586, Université de Lyon I, Université de Lyon, F69622 Villeurbanne, France

5 [‡]INSA Lyon, MATEIS, UMR CNRS 5510, Université de Lyon, F69621 Villeurbanne, France

6 ^{||}Institut Charles Delaunay, LASMIS UMR CNRS 6279, Ecole Polytechnique Féminine, F10004 Troyes, France

7 [§]LIPhy, UMR CNRS 5588, Université Joseph Fourier, Grenoble, F38402 Grenoble, France

8 **ABSTRACT:** Oriented block copolymers exhibit a buckling
9 instability when submitted to a tensile test perpendicular to the
10 lamellae direction. In this paper we study this behavior using a
11 coarse grained molecular dynamics simulation approach.
12 Coarse grained models of lamellar copolymers with alternate
13 glassy rubbery layers are generated using the radical like
14 polymerization method, and their mechanical response is
15 studied. For large enough systems, uniaxial tensile tests
16 perpendicular to the direction of the lamellae reveal the
17 occurrence of the buckling instability at low strain. The results
18 that emerge from molecular simulation are compared to an
19 elastic theory of the buckling instability introduced by Read
20 and co-workers. At high strain rates, significant differences are
21 observed between elastic theory and simulation results for the
22 buckling strain and the buckling wavelength. We explain this difference by the strain rate dependence of the mechanical response.
23 A simple model that takes into account the influence of the strain rate in the mechanical response is presented to rationalize the
24 results at low and moderate strain rates. At very high strain rates, cavitation takes place in the rubbery phase of the sample and
limits the validity of the approach.



I. INTRODUCTION

25 Block copolymers such as (styrene–butadiene–styrene, SBS, or
26 styrene–isoprene–styrene, SIS) have attracted much interest in
27 the past few decades for their use as thermoplastic elastomers.
28 The microstructure of such materials results from the mixture
29 of two different homopolymers. Interesting combination of
30 properties (similar to the case of nanocomposites) at ambient
31 temperature can be obtained when one of the constitutive
32 homopolymer is hard (glassy or crystalline) while the other one
33 is soft (rubbery). As both constituents are linked together by
34 chemical cross-links, the resulting material combines the
35 mechanical properties of each phase: therefore ductility of the
36 rubbery phase is coupled to the toughness of the glassy phase.
37 The mechanical response of such composite materials is far
38 from being understood, especially at the molecular scale.
39 Depending on the amount of each component, the
40 thermodynamics equilibrium between phases leads to various
41 morphologies (e.g., spherical, cylindrical, and lamellar¹). The
42 lamellar morphology is particularly interesting as a model
43 system because the global behavior is not dominated by one of
44 the component. Moreover, the one-dimensional aspect of the
45 lamellar morphology is similar to the morphology of semi-
46 crystalline polymers at small scale.
47 Such nanostructured materials exhibit similar mechanical
48 behavior^{2–5} through complex deformation mechanisms when
49 they are stretched perpendicular to the lamellae direction: the

hard lamellae buckle, forming a “chevron-like” morphology. 50
This phenomenon has been observed in semicrystalline 51
polymers by several authors^{6,7} and more recently by Bartczak 52
and Mohanraj.^{8,9} Buckling of hard lamellae is of prior 53
importance regarding the mechanical properties of nano- 54
structured polymers: it induces a rapid collapse of the hard 55
phase network which can be an initiator of the macroscopic 56
yield, decreasing thus the mechanical properties of the material. 57
Several experimental works^{10–15} were focused on the 58
formation of “chevron” in block copolymers using *in situ* 59
small angle X-ray scattering (SAXS). The results reveal a 60
progressive modification of the SAXS pattern at yield, from two 61
spots to four symmetric spots, which is the signature of the 62
“chevron” morphology (see Figure 1). 63 fi
Buckling was also observed by a direct examination of the 64
microstructure of highly deformed SBS samples using atomic 65
force or electron microscopy.^{16,17} The origin of buckling is 66
interpreted from the contrast in the elastic properties of the 67
glassy and rubbery layers. As the rubbery layer accommodates 68
most of the imposed deformation, it tends to contract in the 69
transverse direction. The strong coupling between phases leads 70
to a compressive stress in the transverse direction of the glassy 71

Received: March 12, 2013
Revised: September 10, 2013

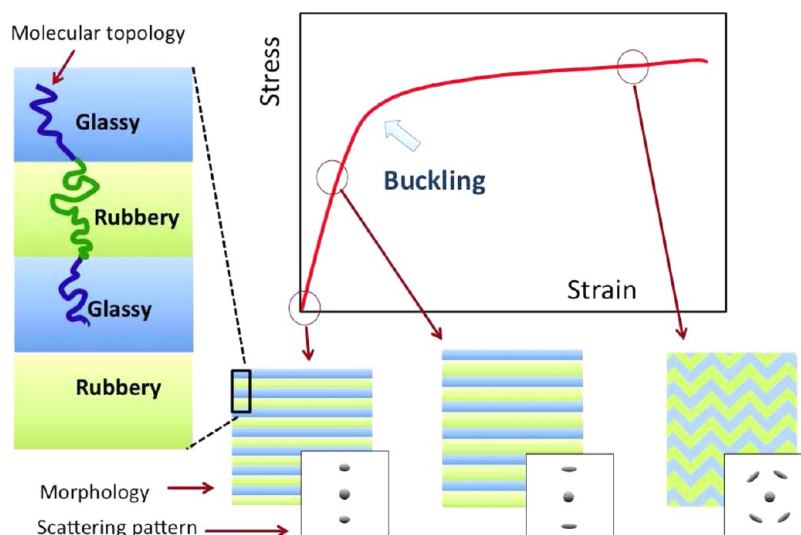


Figure 1. Schematic description: Evolution of a triblock morphology from lamellar to chevron-like morphology under tensile test conditions. This transformation separates two regimes: (i) the elastic regime; (ii) the buckling regime. A schematic description of the phases topology is shown at left. The corresponding SAXS patterns are shown in the inset.

72 layer. As a consequence, the glassy lamellae buckle to form a
73 “chevron” morphology.

74 These qualitative explanations are well established. How-
75 ever, the attempts to model the phenomenon theoretically are
76 scarce, and essentially at the level of a continuum description.
77 In a pioneering work, Read et al.¹⁸ proposed an original
78 energetic approach to describe the competition between
79 buckling and affine deformation, and proved with finite
80 element methods (FEM) that this instability can occur even
81 in the pure elastic regime. Unfortunately, this purely elastic
82 approach ignores visco-elastic or rate dependent effects, and
83 does not account for the competition with other failure modes
84 such as cavity nucleation.

85 In this paper, we study the initiation of the buckling
86 instability and the mechanical response of a block copolymer
87 model using coarse grained molecular dynamics simulations.
88 This numerical tool is indeed particularly adapted to study this
89 problem as it intrinsically contains elasticity, viscosity, and all
90 associated dynamical effects. It also accounts for defects, and for
91 the different coupling strengths that can exist between phases,
92 depending on the density of tie molecules.¹⁹ Moreover, coarse
93 grained MD permits the study of buckling well above the yield
94 stress in the plastic regime, where other instabilities such as
95 cavitation can occur.²⁰ The approach gives access to the local
96 measurement of many variables (e.g local stress, local density)
97 while monitoring the global mechanical behavior. This allows
98 one to investigate the relationship between the mechanical
99 response and the change in the local microstructure and
100 morphology.

101 This paper is a companion paper of a previously published
102 report,²¹ which showed the feasibility of such an approach and
103 gave a preliminary account of the results. Section II presents the
104 model and the methods that are used in this study. Section III
105 discusses the relationship between the microstructure and the
106 associated stress–strain curve. Section IV recalls the formalism
107 introduced by Read et al.¹⁸ The following sections detail the
108 effect of sample size (section V) and strain rate (section VI). A
109 simple kinetic model predicting the competition between
110 buckling modes is finally presented in section VII and
111 compared with MD results.

II. METHOD AND MODEL

The Molecular Dynamics Model. Molecular dynamics 112
(MD) simulations were carried out for a well established 113
coarse-grained model,²² in which the polymer is treated as a 114
chain of N beads, which we refer to as monomers, of mass $m =$ 115
1 connected by a spring to form a linear chain. The beads 116
interact with a classical Lennard-Jones (LJ) interaction: 117

$$U_{\text{LJ}}^{\alpha\beta}(r) = \begin{cases} 4\epsilon_{\alpha\beta} \left[\left(\frac{\sigma_{\alpha\beta}}{r} \right)^{12} - \left(\frac{\sigma_{\alpha\beta}}{r} \right)^6 \right], & r \leq r_c \\ 0, & r > r_c \end{cases} \quad (1) \quad 118$$

where the cutoff distance $r_c = 2.5\sigma$. α and β represent the 119
chemical species (i.e., A and B) In addition to (1), adjacent 120
monomers along the chains are coupled through the well- 121
known anharmonic finite extensible nonlinear elastic potential 122
(FENE): 123

$$U_{\text{FENE}}(r) = -0.5kR_0^2 \ln \left[1 - \left(\frac{r}{R_0} \right)^2 \right], \quad r \leq R_0 \quad (2) \quad 124$$

The parameters are identical to those given in Kremer et al.,²² 125
namely $k = 30\epsilon/\sigma^2$ and $R_0 = 1.5\sigma$, chosen so that unphysical 126
bond crossings and chain breaking are avoided. All quantities 127
will be expressed in terms of length σ , energy ϵ , pressure ϵ/σ^3 128
and time $\tau = (m\sigma^2/\epsilon)^{1/2}$. 129

Newton’s equations of motion are integrated with the 130
velocity Verlet method and a time step $\Delta t = 0.006\tau$. Periodic 131
simulation cells containing $340 \times n$ chains (n is the replication 132
number—see below) of $N = 200$ beads were used with a 133
Nosé–Hoover barostat, i.e. in the NPT ensemble. An 134
anisotropic barostat with $P_x = P_y = P_z = 0$ is used in the 135
equilibration, leading to a tetragonal simulation box before 136
running the tensile test. 137

Polymer Sample Generation. Our samples have been 138
generated using the “radical-like polymerization” (RLP) 139
method.²³ The polymerization takes place in a LJ liquid bath 140
(solvent) for which $\epsilon_{\alpha\beta} = 1$ ϵ and $\sigma_{\alpha\beta} = 1$ σ for all LJ 141
interactions. A set of 340 monomers are chosen as “radicals”. 142

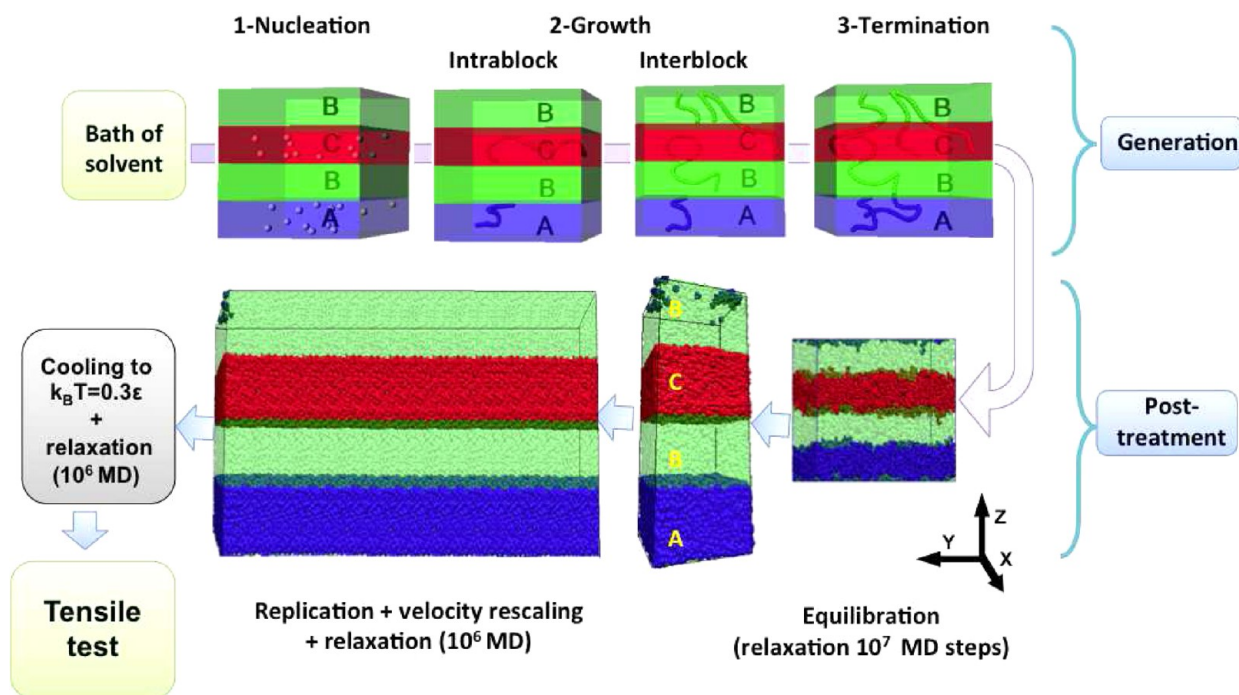


Figure 2. Schematic description of the generation and the post treatment process. Starting from a bath of monomers (“solvent”), the radical like polymerization routine will transform the single disconnected beads to entangled chains. The polymerization occurs in four blocks A, B, C, and B. The resulting chains are shared between three successive blocks A, B, and C. LJ interaction energies are chosen so that a perfect segregation of the blocks is ensured at low temperature.

143 The growth of chains is then performed by a sequence of bead-
144 addition (growth) and subsequent relaxation. In the growth
145 stage, each radical captures one of its free nearest neighbors and
146 a covalent bond is created between them. The newly bonded
147 monomer becomes itself a radical. After that, the system is
148 relaxed during 500 MD steps at $k_B T = 1 \epsilon$. Then, a new growth
149 step is performed, until chains reach the desired size.

150 This concept was adapted to generate triblock copolymer
151 samples with four distinct blocks ABCB and four interfaces
152 parallel to the (xy) plane. The generation starts simultaneously
153 in blocks A and C. When the chains reach a length of $N/4$, the
154 radical is dragged toward the nearest interface to complete the
155 growth of chain in neighboring blocks B. After the chain
156 reaches a length of $3N/4$, the radical, that started growth in
157 block A moves to achieve the polymerization in block C and
158 *vice versa*. The generation is stopped when all chains attain the
159 request length N . The generation method is detailed in
160 references.^{19,23}

161 **Equilibration and Replication.** After the sample has been
162 generated, the remaining solvent is removed from the
163 simulation box. The LJ interaction energies are then adjusted
164 to drive the segregation and associated block thickness. In this
165 study, the LJ energies are chosen such that A and C layers are
166 glassy, while B layer is rubbery: $\epsilon_{AA} = \epsilon_{CC} = 1 \epsilon$, $\epsilon_{BB} = 0.3 \epsilon$ and
167 $\epsilon_{AB} = \epsilon_{BC} = 0.4 \epsilon$. The system is then relaxed 10^7 MD steps in
168 NPT ensemble at $k_B T = 1 \epsilon$. All the pressure components are
169 maintained at zero ($P_x = P_y = P_z = 0$) using an anisotropic
170 barostat, allowing box changes in the three dimensions
171 independently. The evolution of the box lengths during the
172 relaxation steps has been measured and it has been found that
173 the box dimensions reach a steady state after 10^7 MD steps,
174 indicating that mechanical equilibrium is reached.

175 In order to study the effect of sample size, larger samples
176 were built by replicating several times the basic periodic sample

in the y direction. The replication was performed at $k_B T = 1 \epsilon$
177 where the two phases are rubbery. To avoid unphysical internal
178 periodicity, bead velocities are rescaled and an additional 10^6
179 MD steps are performed. After this relaxation stage, each
180 sample is cooled down to a temperature of $k_B T = 0.3 \epsilon$ during 7
181 $\times 10^5$ MD steps and relaxed again 10^6 MD steps. Four different
182 box sizes (in the y direction) have been investigated: 200, 400,
183 500, and 800 σ .
184

185 Finally, the glass transition temperatures of each phase were
186 determined from volume curves at constant pressure, and it was
187 found that $T_g^A = 0.43$ and $T_g^B = 0.20$. In the following the system
188 will be studied at a temperature intermediate between T_g^A and
189 T_g^B , so that the B phase has the properties of a rubber and the A
190 phase those of a glass. Figure 2 describes schematically the
191 sequence operations for both generation and post treatment
192 stages of the sample.

193 **Tensile Test.** To deform our samples, uniaxial homoge-
194 neous tensile test conditions were employed.²⁰ The samples
195 were subjected to a sequence of deformation-relaxation steps,
196 composed of the following: (i) a rescaling of the simulation box
197 in the tensile direction (Z in our case, so that the true strain is
198 $\epsilon_{ZZ} = \ln(L_Z(t)/L_Z(0))$); and, (ii) one MD step in the NPT
199 ensemble at $k_B T = 0.3 \epsilon$ and $P_x = P_y = 0$ (Nosé–Hoover
200 anisotropic barostat is employed to control the pressure only in
201 x and y directions independently). The tensile velocity \dot{L}_Z was
202 chosen so that the initial strain rate is $\dot{\epsilon}_{yy}(0) = 7.3 \times 10^{-5} \tau^{-1}$
203 (high strain rate tests) and $\dot{\epsilon}_{yy}(0) = 1.4 \times 10^{-5} \tau^{-1}$ (low strain
204 rate tests).

III. STRESS/STRAIN CURVE

205 In order to study the correlation between the mechanical
206 response and the change of the sample morphology, we start by
207 presenting the results of uniaxial tensile tests on “large” ($L_Y \approx$
208 400σ) samples. The tensile strain was applied in the Z direction

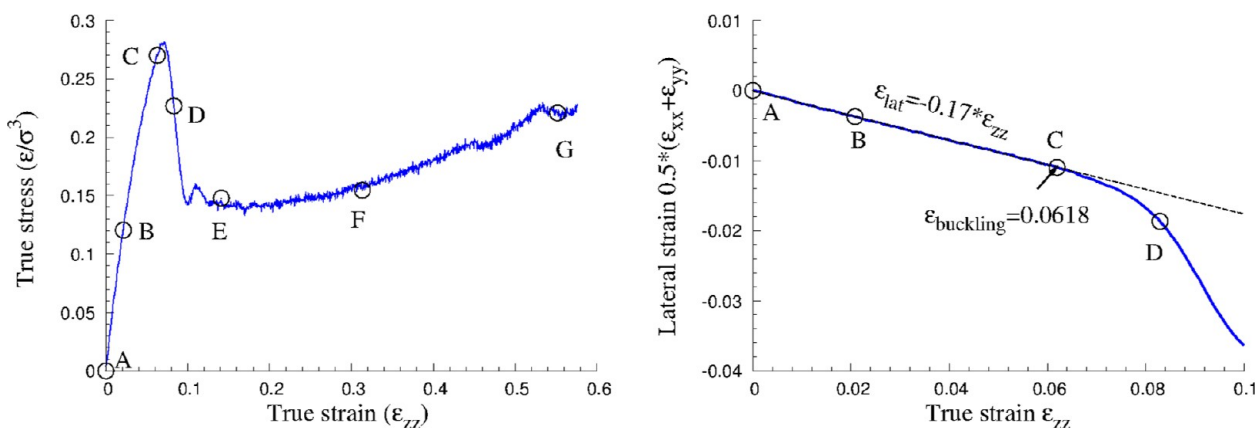


Figure 3. Left: Stress strain curve of a sample submitted to a uniaxial tensile test in the direction normal to the layers (Z direction). The black circles correspond to the density maps shown in Figure 4. Right: Lateral strain in the same sample with respect to the tensile strain. The first linear part of the curve fits the Poisson ratio of the sample in the elastic regime. The curve deviates from this linear behavior after buckling has occurred.

209 (perpendicular to the lamellae) at a constant velocity $V_z = \dot{L}_z$.
 210 In this first set of results, the strain rate is $\dot{\epsilon}_{zz} = 7.3 \times 10^{-5} \tau^{-1}$
 211 and the initial size of the simulation box is $(32.4 \times 74.2 \times$
 212 $393.6) \sigma^3$. The resulting stress–strain curve is plotted in Figure
 213 3. During the tensile test, sample configurations were stored at
 214 different strains. Figure 4 shows the local density map of such
 215 configurations, where the glassy and the rubbery phases can be
 216 distinguished by the high and low density lamellae, respectively.

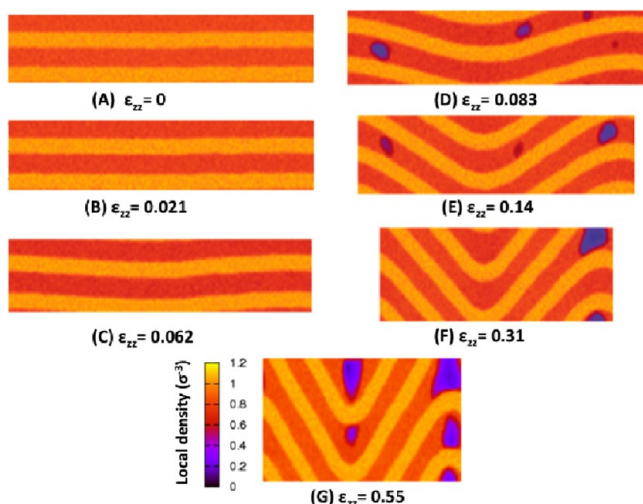


Figure 4. Local density cartography of the tested sample at several strains. The color contrast illustrates the alternance of glassy and rubbery lamellae with high and low density, respectively. As the deformation progresses, nucleation of cavities occurs randomly in the rubbery phase. Cavities that are located in the tilted part of the chevron disappear, as the deformation in these regions becomes a simple shear deformation; however, only cavities that are located in the hinges, where the deformation is effectively triaxial, persist to a high strain.

217 The stress–strain curve in Figure 3 exhibits different regimes.
 218 In the first elastic regime the stress growth linearly. This
 219 response results from the serial coupling of the lamellae and the
 220 imposed strain is mainly accommodated by the deformation of
 221 the soft phase (rubbery). Beyond the elastic regime a
 222 progressive softening is observed. This softening is correlated
 223 to a progressive change in the morphology of the sample, as the
 224 aligned lamellae start to buckle, leading to an undulated pattern.

Buckling is signaled by a drastic change of the apparent Poisson
 225 ratio, illustrated in Figure 3, right, which displays the lateral
 226 strain as a function of the imposed normal strain. The first
 227 linear part of the curve corresponds to the linear elastic regime,
 228 and the slope gives the apparent Poisson ratio of the sample.
 229 A sudden decrease of the Poisson ratio appears when the buckling
 230 starts. After the onset of buckling, cavities nucleate in the
 231 rubbery phase, leading thus to a strong drop in the stress.
 232 Figure 4 shows the nucleation and the evolution of the cavities
 233 (low density spots in the rubbery phase). With increasing strain
 234 the amplitude of the buckling undulation develops. The cavities
 235 that are first randomly nucleated in the rubbery phase, become
 236 progressively localized at the hinges of the pattern. Indeed,
 237 cavities nucleated in the tilted part of the buckle tend to heal, as
 238 the stress in these regions becomes a simple shear. On the
 239 contrary, the stress at the hinges is essentially triaxial, and favors
 240 cavitation.

The micromechanical origin of buckling instability has been
 242 elucidated in ref 21. Because of the serial coupling between the
 243 glassy and rubbery phases, the tensile strain will be mainly
 244 localized in the rubbery lamellae. The tensile strain in the
 245 normal direction of the layers will be converted locally to a
 246 contraction in the transverse direction because of the Poisson
 247 effect in the rubber. This lateral contraction will be transmitted
 248 to the glassy phase via the interface, then a compressive stress
 249 acts on the transverse direction of the glassy lamellae. Under
 250 these conditions, and for a sufficiently large system, a buckling
 251 instability takes place to relax the lateral compressive stress.

IV. THEORETICAL MODELING OF BUCKLING INSTABILITY

The development of a buckling instability in a layered material
 254 with alternative hard and soft blocks can be studied using
 255 elasticity theory. The volume average elastic energy density of a
 256 homogeneously strained sample is, as usual, given by

$$\langle e \rangle = \frac{1}{2} C_{ijkl} \langle \epsilon_{ij} \epsilon_{kl} \rangle \quad (3)$$

where ϵ_{ij} are the components of the macroscopic strain, and
 259 C_{ijkl} the elastic constants. For the sake of simplicity, only a 2D
 260 case is presented here: the x direction is parallel to the lamellae,
 261 and z the direction of traction, perpendicular to the lamellae.
 262 Taking into account the symmetry of our system (transversely 263

264 isotropic—see eq 2), the volume averaged elastic energy
265 density reduces to

$$2\langle e \rangle = C_{11}\langle \epsilon_{11}^2 \rangle + C_{33}\langle \epsilon_{33}^2 \rangle + 2C_{13}\langle \epsilon_{33}\epsilon_{11} \rangle + 2C_{44}\langle \epsilon_{13}^2 \rangle \quad (4)$$

266 where standard Voigt notations have been used. Here the
267 energy density is expressed in a local frame that is aligned with
268 the lamellar pattern, as will become clear below. The elastic
269 constants are the effective values that describe the lamellar
270 material as a whole, and depend from the characteristics of each
271 phase. A particularity of the dibloc material resides in the values
272 of these elastic constants (see Table 1). The material is

Table 1. Elastic Constants of the Layered Bock Copolymer Studied in This Paper^a

	C_{11}	C_{33}	$C_{23} = C_{13}$	$C_{44} = G$	ν
$[\epsilon/\sigma^3]$	24	7.6	6.5	0.07	0.18

^aElastic constants have been determined with molecular statics on a stress-free sample by applying small perturbation in the box shape. For the sake of comparison, the Young modulus of a glassy polymer is of order $50 \epsilon/\sigma^3$.

274 remarkably soft when submitted to shear in the xz or yz
275 directions. Therefore, when submitted to a tensile stress in the
276 z direction, the material will have a tendency to locally rotate in
277 order to align its soft directions at 45° from the direction of
278 traction.

279 The formalism of eq 4, which assumes a homogeneous strain,
280 is not appropriate to predict such a rotation, and in principle a
281 full finite element calculation involving space varying elastic
282 constants appropriate for the different phases would be
283 required. The analysis proposed by Read et al.¹⁸ bypasses this
284 difficulty, by describing the local deformation of the sample ϵ_{ij}
285 as a combination of a “shear + strain” deformation expressed in
286 the local frame of the lamellae (through ϵ_{11} , ϵ_{13} , and ϵ_{33} —
287 transformation matrix $[S]$) with a space dependent rotation θ
288 (transformation matrix $[R]$, which describes the local tilt of the
289 lamellar structure. The two transformation matrixes that
290 describe these deformations are:

$$[R] = \begin{bmatrix} \cos \theta & -\sin \theta \\ \sin \theta & \cos \theta \end{bmatrix} \quad \text{and} \quad [S] = \begin{bmatrix} 1 + \epsilon_{11} & \epsilon_{13} \\ 0 & 1 + \epsilon_{33} \end{bmatrix} \quad (5)$$

292 Under deformation, two adjacent points $M_0(x_0, z_0)$ and $M(x_0$
293 $+ \delta x, z_0 + \delta z)$ are transformed into $M'_0(x'_0, z'_0)$ and $M'(x'_0 +$
294 $\delta x', z'_0 + \delta z')$, and the vector \mathbf{MM}_0 experiences the
295 combination of the rotation and deformation:

$$\mathbf{M}'\mathbf{M}'_0 = [R][S]\mathbf{M}\mathbf{M}_0 \quad (6)$$

297 In terms of the coordinates, this reads

$$\begin{pmatrix} \delta x' \\ \delta z' \end{pmatrix} = \begin{bmatrix} \cos \theta & -\sin \theta \\ \sin \theta & \cos \theta \end{bmatrix} \begin{bmatrix} 1 + \epsilon_{11} & \epsilon_{13} \\ 0 & 1 + \epsilon_{33} \end{bmatrix} \begin{pmatrix} \delta x \\ \delta z \end{pmatrix} \quad (7)$$

299 If one now introduces the displacement field $\mathbf{v}(x, z)$ such
300 that $\mathbf{M}'_0 = \mathbf{M}_0 + \mathbf{v}(x_0, z_0)$, the relation between $\mathbf{M}'\mathbf{M}'_0$ and
301 $\mathbf{M}\mathbf{M}_0$ is expressed in terms of the displacement gradients:

$$\begin{pmatrix} \delta x' \\ \delta z' \end{pmatrix} = \begin{pmatrix} \delta x \\ \delta z \end{pmatrix} + \begin{bmatrix} \nabla_x v_x & \nabla_z v_x \\ \nabla_x v_z & \nabla_z v_z \end{bmatrix} \begin{pmatrix} \delta x \\ \delta z \end{pmatrix} \quad (8)$$

Combining eqs 7 and 8 leads to a system of 4 equations that
303 can be inverted to give θ , ϵ_{11} , ϵ_{13} and ϵ_{33} in terms of the
304 displacement gradient ∇v :
305

$$\begin{cases} \sin \theta = \nabla_x v_z / \Delta \\ \epsilon_{11} = \Delta - 1 \\ \epsilon_{33} = [(1 + \nabla_z v_z)(1 + \nabla_x v_x) - \nabla_z v_x \nabla_x v_z] / \Delta - 1 \\ \epsilon_{13} = [(\nabla_z v_x)(1 + \nabla_x v_x) + (\nabla_x v_z)(1 + \nabla_z v_z)] / \Delta \end{cases} \quad (9)$$

where $\Delta = ((\nabla_x v_z)^2 + (1 + \nabla_x v_x)^2)^{1/2}$. Note that if the sample
307 is submitted to pure shear, such as only $\nabla_x v_z \neq 0$, $\sin \theta = \epsilon_{13}$;
308 i.e., the shear is completely described by the local rotation.
309

In order to describe an undulating pattern of the lamellar
310 structure, the global displacement vector v is decomposed in
311 two contributions: the macroscopic deformation of the sample
312 (strains ϵ_{xx} , ϵ_{zz} , and ϵ_{zz}) and a small perturbation that imposes a
313 displacement along z only: $\mathbf{u} = u_z(x)\mathbf{z}$.
314

$$\begin{cases} v_x = \epsilon_{xx}x \\ v_z = \epsilon_{zz}z + u_z \end{cases} \quad (10)$$

where $u_z(x) = U_0 \sin(kx)$ is a sinusoidal small perturbation of
316 wave vector k that describes the local displacement due to
317 buckling.
318

Now, it is possible to calculate local deformations ϵ_{11} , ϵ_{13} and
319 ϵ_{33} of eq 11 using the decomposition described in eq 10. Only
320 second order terms of the small sinusoidal perturbation U_0 are
321 retained, leading to the following expressions for the local
322 deformations in the frame of the lamellae:
323

$$\begin{cases} \langle \epsilon_{11}^2 \rangle = \epsilon_{xx}^2 + \frac{U_0^2 k^2}{2(1 + \epsilon_{xx})^2} \epsilon_{xx}(1 + \epsilon_{xx}) \\ \langle \epsilon_{33}^2 \rangle = \epsilon_{zz}^2 - \frac{U_0^2 k^2}{2(1 + \epsilon_{xx})^2} \epsilon_{zz}(1 + \epsilon_{zz}) \\ \langle \epsilon_{11}\epsilon_{33} \rangle = \epsilon_{xx}\epsilon_{zz} + \frac{U_0^2 k^2}{4(1 + \epsilon_{xx})^2} (\epsilon_{zz} - \epsilon_{xx}) \\ \langle \epsilon_{13}^2 \rangle = \frac{U_0^2 k^2}{2(1 + \epsilon_{xx})^2} (1 + \epsilon_{zz})^2 \end{cases} \quad (11)$$

It is worth noting that, for a tensile test along the z axis ($\epsilon_{xx} < 0$
325 and $\epsilon_{zz} > 0$), the rotation introduced previously induces a net
326 decrease in the squared local deformations, leading to an energy
327 relaxation and demonstrating thus the possibility for an
328 instability.
329

Inserting the identities above into the energy density eq 4
330 leads to the volume averaged elastic energy density:
331

$$2\langle e \rangle = C_{11}\epsilon_{xx}^2 + 2C_{13}\epsilon_{xx}\epsilon_{zz} + C_{33}\epsilon_{zz}^2 + \frac{1}{2}U_0^2 k^2 f_1^{2D} \quad (12)$$

where

$$f_1^{2D} = [G - \epsilon_{zz}(C_{33} - C_{13} - 2G) - \epsilon_{zz}^2(C_{33} - G) + \epsilon_{xx}(C_{11}(1 + \epsilon_{xx}) - C_{13})]/(1 + \epsilon_{xx})^2 \quad (13)$$

Because of the specific moduli of our composite system (see
335 Table 1), the term f_1^{2D} , slightly positive at zero strain, rapidly
336

337 turns negative as strain increases (*i.e.*, after less than 1%
338 deformation in z). Thanks to this combination of trans-
339 formations, the local shear in the xz plane is completely
340 handled by the rotation θ , decreasing the elastic energy of the
341 system and causing thus the buckling instability.

342 However, in eq 12, there is no cost associated with the
343 sinusoidal bending of the material, except the shearing of the
344 soft phase, which is, as mentioned previously, very low. In order
345 to account for the energy associated with the bending of the
346 composite, and particularly the bending of the hard phase, a
347 new term has to be added. It is assumed here, following the idea
348 of Read et al., that only the hard layers contribute to the
349 bending energy. A macroscopic expression is then introduced
350 from beam mechanics, which gives the energy, that is necessary
351 to bend a plate:

$$352 \quad e_b = \frac{1}{2} K (\nabla_x \theta)^2 \quad (14)$$

353 where K is the bending modulus of the sample. Because of the
354 serial coupling between phases the bending modulus will be
355 dominated by the contribution of the hard phase. The bending
356 modulus can then be estimated from simple beam bending
357 theory as $K = (\phi_h^3 E_h d^2) / ([12(1 - \nu_h^2)])$ where ϕ_h is the volume
358 fraction of the hard phase, E_h and ν_h are the Young's modulus
359 and Poisson ratio of the hard phase and d is the lamellar
360 spacing.

361 The total energy density results from the addition of the bulk
362 elastic energy and the bending energy, $\langle e_T \rangle = \langle e_b \rangle + \langle e \rangle$:

$$363 \quad 2\langle e_T \rangle = C_{11}\epsilon_{xx}^2 + 2C_{13}\epsilon_{xx}\epsilon_{zz} + C_{33}\epsilon_{zz}^2 + F(\epsilon_{zz}, k) \quad (15)$$

364 with $F(\epsilon_{zz}, k) = (U_0^2/2)(k^2 f^{2D} + Kk^4)$. In the real 3D case,
365 the same analysis can be performed, which leads to a function
366 f^{3D} instead of f^{2D} where:

$$367 \quad f^{3D} = f^{2D} - \frac{C_{23}\epsilon_{yy}}{(1 + \epsilon_{xx})^2} \quad (16)$$

368 This leads to the final form of the function $F(\epsilon_{xx}, \epsilon_{yy}, \epsilon_{zz}, k)$:

$$369 \quad F(\epsilon_{xx}, \epsilon_{yy}, \epsilon_{zz}, k) = \frac{U_0^2}{2} (k^2 f^{3D} + Kk^4) \quad (17)$$

370 The buckling instability occurs upon increasing strain when
371 the function $F(\epsilon_{xx}, \epsilon_{yy}, \epsilon_{zz}, k)$ in eq 15 becomes negative,
372 meaning that the global gain in elastic energy overwhelms the
373 bending energy penalty.

374 Finally, before the buckling begins (*i.e.*, in the elastic regime)
375 ϵ_{xx} and ϵ_{yy} can be replaced by $\nu\epsilon_{zz}$ where ν is a global Poisson
376 ratio. Under this assumption, $f^{3D}(\epsilon_{xx}, \epsilon_{yy}, \epsilon_{zz})$ becomes $f^{3D}(\epsilon_{zz})$
377 and $F(\epsilon_{xx}, \epsilon_{yy}, \epsilon_{zz}, k)$ becomes $F(\epsilon_{zz}, k)$.

378 Figure 5 shows the evolution of $F(\epsilon_{zz}, k)$ as a function of the
379 wave vector k for several tensile strains ϵ_{zz} . At low strain $F(\epsilon_{zz}, k)$
380 k_n) is positive for any possible wave vector k , therefore the
381 buckling is impossible. As the tensile strain increases $F(\epsilon_{zz}, k_n)$
382 becomes negative for a wave vector range, which indicates the
383 possibility of buckling.

384 Note that the periodic boundary conditions imposed in the
385 direction y in our MD simulations limit the possible
386 wavevectors to the discrete set:

$$387 \quad k = k_n = n \frac{2\pi}{L_y} \quad (18)$$

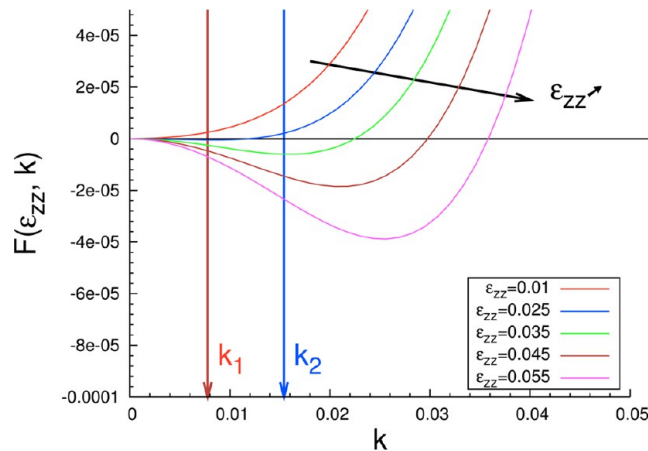


Figure 5. Evolution of $F(\epsilon_{zz}, k)$ (see eqs 15 and 17) for different levels of strain, the two arrows denote the wavevectors $k_1 = 2\pi/L_y$ and $k_2 = 4\pi/L_y$.

where n is the mode number; *i.e.*, $n = 1$ is the fundamental
388 mode where the wavelength of the perturbation is equal to the
389 sample size. Figure 5 shows that as deformation increases, the
390 first wavelength for which the sinusoidal perturbation might be
391 stable is the fundamental one. As the deformation increases, the
392 fundamental mode might not be the most energetically
393 favorable, since larger wave vectors lead to more negative
394 values for $F(\epsilon_{zz}, k_n)$.

Finally, buckling occurs if:

$$395 \quad f^{3D}(\epsilon_{zz}) + K \left(n \frac{2\pi}{L_y} \right)^2 < 0 \quad (19) \quad 397$$

Resolution of eq 19 leads to a prediction of the strain at
398 which bucking should appear as a function of sample length L_y ,
399 for a given mode n (see 10).

In the next section, we present a comparison between our
401 MD simulations and this linear stability analysis. 402

V. INFLUENCE OF THE SAMPLE SIZE

According to the elastic theory, the instability will take place at
403 smaller strains for bigger samples, and always at the largest
404 possible wavelength allowed by the boundary conditions. We
405 have therefore studied several samples with different sizes. 406
These samples were created by replicating the *same* elementary
407 cell i times along the Y direction, where $i = 3, 6, 12, 15,$ and 24
408 times. Because of the periodic boundary conditions, the
409 buckling wavelength must be an integer subdivision of the
410 sample size, $k_n = n \times (2\pi/L_y)$. 411

Figure 6 compares the mechanical response of all tested
412 samples, at the same strain rate $\dot{\epsilon}_{zz} = 7.3 \times 10^{-5}$. In terms of
413 stress-strain relation (Figure 6a), all samples have roughly the
414 same mechanical response up to the yield point. The drawing
415 regimes exhibits important differences between smaller and
416 larger samples. The stress softening in large samples is more
417 pronounced than in the small ones. Indeed, both cavitation and
418 buckling can limit the stress growth of the elastic regime,
419 leading then to a stress drop. For long samples, the two
420 mechanisms participate in the stress softening, thus the drop of
421 stress will be increased compared to the short sample case
422 where only cavitation is present. 423

The right panel in Figure 6 shows the lateral strain in the
424 different samples. All curves fit very well the same Poisson ratio 425

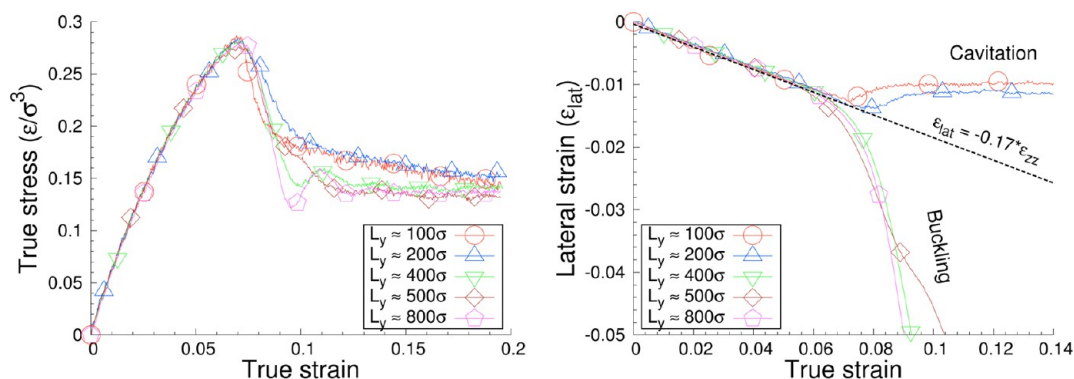


Figure 6. Left: Comparison between the mechanical responses of several samples with different sizes, the strain rate is $\dot{\epsilon}_{zz} = 7.3 \times 10^{-5}$ for all samples. The corresponding lateral strain curves are shown in the right panel. All curves have the same yield point; however, the largest three samples exhibit buckling while only cavitation is present in the two smaller samples. (see the snapshots in Figure 9). When buckling is observed, the buckling strain is roughly independent of sample size, which is in contrast with the prediction from elastic theory.

Length (σ)	Strain rate	Snapshot strain	Snapshot label	Snapshot
≈ 800	1.4×10^{-5}	0.06	s1	
	7.3×10^{-5}	0.08	s2	
≈ 500	1.4×10^{-5}	0.063	s3	
	7.3×10^{-5}	0.08	s4	
≈ 400	1.4×10^{-5}	0.08	s5	
	7.3×10^{-5}	0.08	s6	
≈ 200	1.4×10^{-5}	0.12	s7	
	7.3×10^{-5}	0.12	s8	

Figure 9. Snapshots show several samples under a uniaxial tensile tests driven by two different strain rates $\dot{\epsilon}_{yy} = 7.3 \times 10^{-5}$ and $\dot{\epsilon}_{zz} = 1.4 \times 10^{-5}$. Several lengths are presented, at low strain rate all samples buckle. The buckling wavelength is equal to the sample length. At high strain rate, the buckling wavelength seems to be independent from the sample length. The labels correspond to those indicated in Figure 8.

426 in the first linear part (dashed line). After the yield strain,
 427 strong deviations can be observed: the lateral strain decreases
 428 for long samples ($L_y \geq 393.6\sigma$) while it increases for the shorter
 429 ones ($L_y \leq 196.8\sigma$). The decrease in lateral strain is related to
 430 buckling instability, as described previously. For short samples,
 431 the increase of lateral strain after the yield is correlated with the
 432 nucleation of cavities in the rubbery phase. The buckling in
 433 such samples is completely absent, as shown in the snapshots of
 434 Figure 9.

435 Examining the behavior of the different samples, one
 436 concludes that the minimal length for observing buckling
 437 before cavitation is between $196.8 \leq L_y^* \leq 393.6$. For samples

larger than 393.6σ , the onset of buckling occurs always at the
 same strain ($\epsilon_{buck} = 0.06$), in contradiction with the expectation
 from the elastic description of the previous section. A tentative
 explanation of this behavior will be given below, when we study
 the influence of the strain rate. Another surprising observation,
 illustrated in Figure 9, is that the wavelength of the instability
 does not appear to increase with the size of the system, again in
 contradiction with the expectation from elastic theory.

VI. MECHANICAL BEHAVIOR AT LOWER STRAIN RATE

The observations from the section show a difference between
 the predicted buckling strain and the measures made by

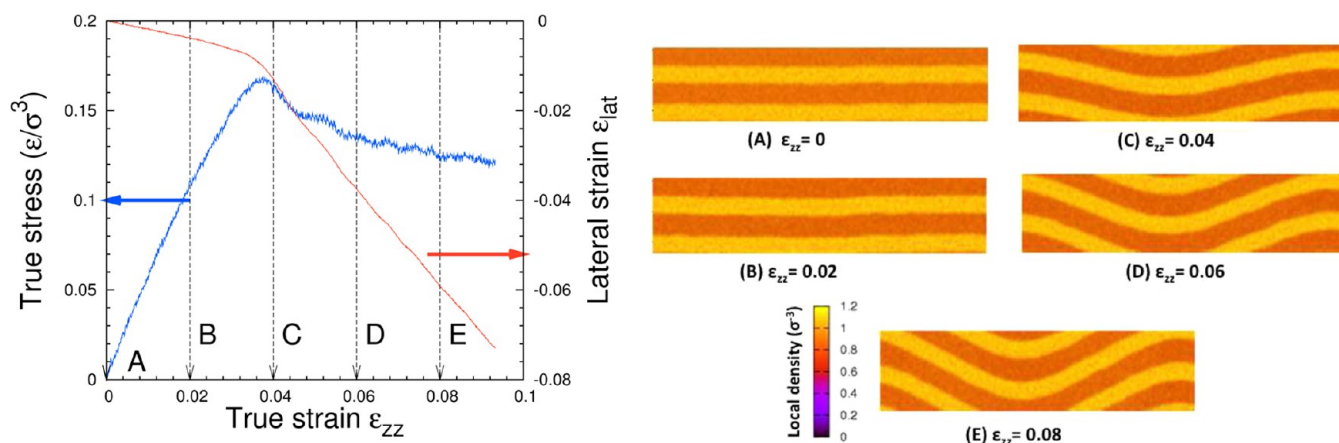


Figure 7. Low strain rate tensile test: the upper panel shows the stress strain curve for the same sample illustrated in Figure 3, together with the evolution of s , the lateral strain. In this case, the yield corresponds to the onset of the buckling. The arrows indicate the strain levels at which the snapshots presented in the lower panel are taken. Cavities are completely absent from the rubbery phase.

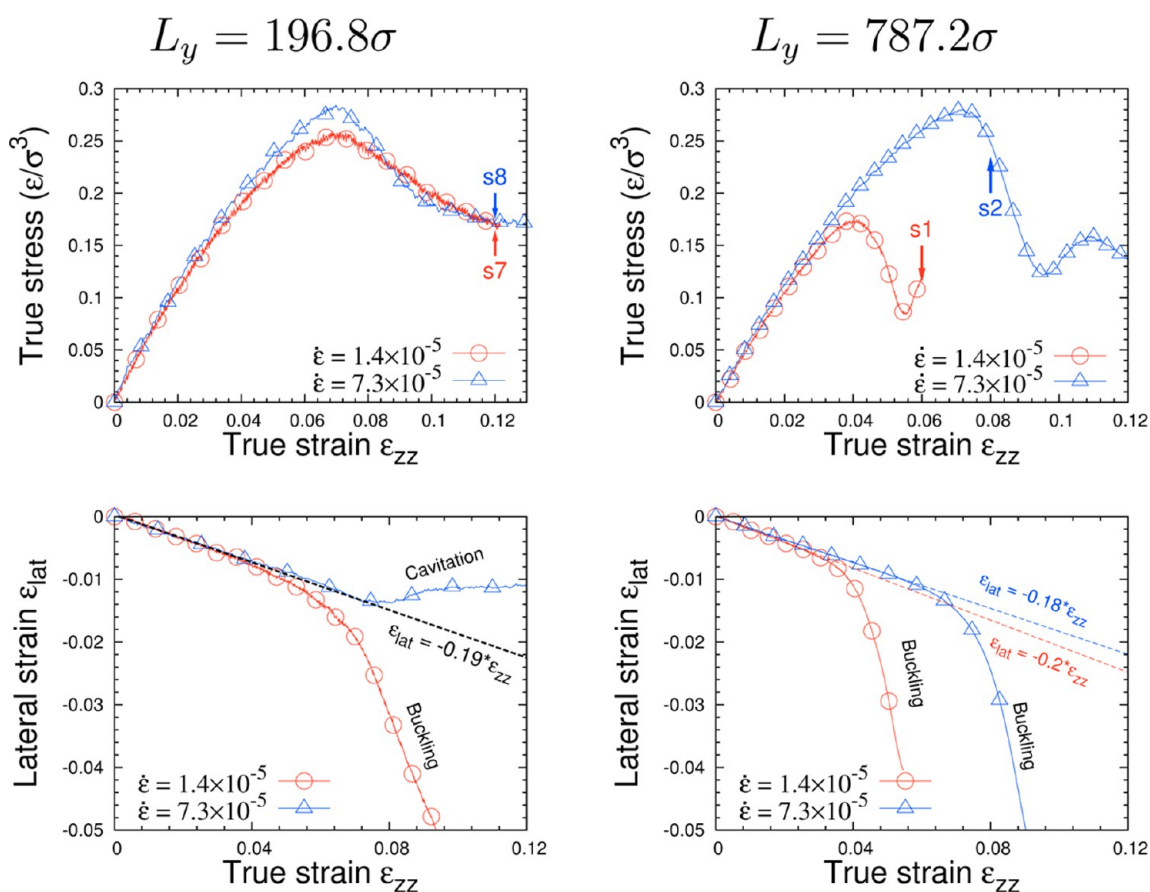


Figure 8. Upper panel: stress–strain curves of the largest and the shortest samples compared at two different strain rates $\dot{\epsilon}_{zz} = 7.3 \times 10^{-5}$ and $\dot{\epsilon}_{zz} = 1.4 \times 10^{-5}$, the lateral strain curves are shown in the lower panel. For the largest sample, decreasing the strain rate will decrease the yield and the buckling strain. This behavior is correlated to the change of the buckling mode as illustrated in Figure 9. For the shortest sample, the behavior changes from cavitation to buckling (see Figure 9).

448 simulation. In order to interpret this difference, we inspect in
 449 this section the influence of the strain rate on the mechanical
 450 response. The same samples described in the previous section
 451 will now be submitted to a similar tensile test, at a strain rate
 452 that is smaller by a factor of approximately 5.

453 **Stress–Strain Response.** Figure 7 shows the results of a
 454 tensile test performed under the same conditions as in section,
 455 except for the strain rate which is 5 times smaller, $\dot{\epsilon}_{yy} = 1.4 \times$

456 10^{-5} . The resulting stress–strain curve, superimposed with the
 457 evolution of lateral strain, are shown in the top panel. The
 458 linear part of both curves corresponds to the elastic regime (the
 459 stress strain curve fits the Young modulus in this regime and
 460 the lateral strain curve fits the Poisson ratio). The end of this
 461 regime is marked by the yield, followed by a stress softening in
 462 stress–strain curve.

463 The yield point corresponds to the onset of buckling, also
 464 indicated by the change of the apparent Poisson ratio in the
 465 lateral strain curve. The absence of cavities was checked by
 466 inspecting the local density of the sample at different strain
 467 levels. Therefore, the yield and the stress softening in this case
 468 is correlated only to the onset and the development of the
 469 buckling in the sample. The last part of the stress–strain curve
 470 is the drawing regime, that corresponds to the development of
 471 the buckling undulation in an “accordion” like manner. Note
 472 that the range of strain studied here is relatively small, so that
 473 the strain hardening regime is not attained.

474 **Influence of Sample Size and of Strain Rate.** In Figure
 475 8, we compare the stress–strain and the lateral strain curves of
 476 our smaller and larger samples, for the two strain rates under
 477 consideration. Clearly the Young modulus is essentially
 478 independent of system size and strain rate. In contrast, the
 479 yield stress and strain decrease as the strain rate decreases, most
 480 markedly in the larger sample. Finally, the stress softening is
 481 significantly weaker at low strain rate, again especially in the
 482 large sample.

483 In general, the decrease of the yield threshold is strongly
 484 correlated with the change of the plastic deformation mode
 485 from cavitation to buckling (the occurrence of buckling for all
 486 samples at low strain rate is illustrated in Figure 9). Both
 487 cavitation and buckling result in a yield behavior, however the
 488 yielding associated with buckling is much more progressive and
 489 smooth than the one associated with cavitation. For the
 490 smallest sample ($L_y = 196.8\sigma$), the lateral strain curve also
 491 highlights a radical change of the mechanical response form
 492 cavitation to buckling at low strain rate.

493 Figure 9 compares the configurations after buckling, at two
 494 different strain rates. The change of the yield mechanism from
 495 cavitation to buckling is well illustrated in these snapshots
 496 especially for the smallest sample. The second important
 497 observation is that the wavelength becomes equal to the sample
 498 length in all samples at low strain rate. Finally, there are no
 499 cavities present in the rubbery phase of the lower strain rate
 500 configurations, compared to systems deformed at high strain
 501 rate for the same strain. These snapshots confirm that the low
 502 energy buckling mode is adopted by the sample at the lowest
 503 strain rate.

504 Figure 10 compares the buckling strain values predicted from
 505 the elastic theory and the one measured from MD simulation
 506 for all samples at two strain rates. The MD buckling strain is
 507 defined by the value of the strain at which a deviation from the
 508 linear Poisson behavior is detected in the lateral strain. Elastic
 509 theory predictions (19) correspond well to MD simulation
 510 performed at low strain rate, which is not the case with high
 511 strain rate MD simulations.

512 Summarizing these observations, the role of the strain rate
 513 seems to be determinant for the mechanical response of the
 514 sample. Depending on the applied rate of the deformation, the
 515 samples switch between the fundamental and the second mode
 516 of buckling or between the cavitation and buckling. In the next
 517 section, a simple model will be proposed to account for this
 518 dependence of the buckling instability on strain rate.

519 **Unloading Process.** The irreversible aspect of the
 520 deformation was studied by instantaneously unloading the
 521 sample after deforming to different final strains, and monitoring
 522 the subsequent relaxation of the strain. The results of these
 523 relaxation simulations are shown in Figure 11. It is seen that the
 524 process is clearly irreversible only for the largest deformation.
 525 For such deformations, significant cavitation has taken place at

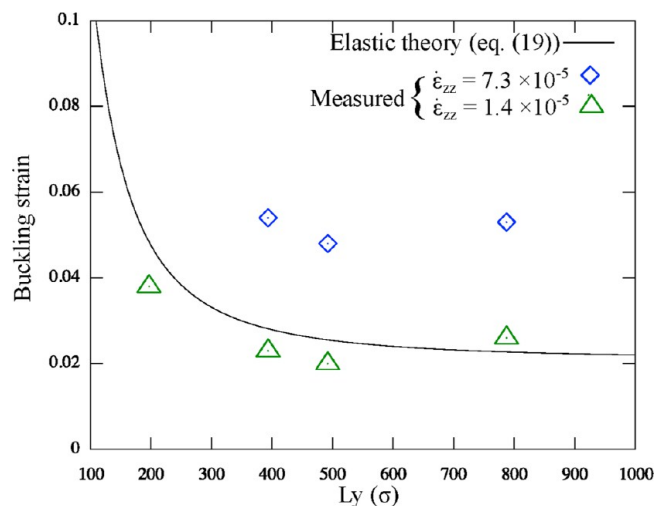


Figure 10. Comparison between the buckling strain values predicted from the elastic theory (19) and the one measured from MD simulations for all samples at two strain rates 7.3×10^{-5} and 1.4×10^{-5} .

526 the hinges of the chevron pattern. The resulting density pattern
 527 under zero load displays a chevron structure with quite large
 528 angles, as observed in experiments. However, the residual,
 529 irreversible deformation is quite small, about 10% for a total
 530 deformation of 50%. This is presumably the consequence of a
 531 model in which the ‘hard’ phase remains in fact relatively soft
 532 (i.e., the contrast in moduli is smaller than in experiments) and
 533 irreversible damage implying chain breaking is excluded. As a
 534 consequence the main source of irreversible damage in the
 535 glassy phase is the cavitation process.

VII. COMPETITION BETWEEN BUCKLING MODES

536 **Modeling.** The results from the previous sections show a
 537 unexpected change of wave vector with strain rate. To
 538 understand this observation, we propose to describe the
 539 growth of the buckling amplitude $U_n(t)$ for a wave vector k_n
 540 = $2n\pi/L_y$ using a simple linear relaxation equation of the form:

$$\frac{dU_n}{dt} = -\Lambda F(\epsilon_{zz}, k_n) U_n \quad (20)$$

541 where $F(\epsilon, k_n) U_n$ is the driving force. Λ is a phenomenological
 542 coefficient which will be assumed to be independent from wave
 543 vector and the strain rate. The solution of this equation can be
 544 written as

$$U_n(t) = U_n(0) \exp\left(-\Lambda \int_0^t F(\epsilon(s), k) ds\right) \quad (21)$$

545 Note that the strain ϵ_{zz} is a time dependent variable $\epsilon_{zz}(t) = \dot{\epsilon}_{zz}$
 546 $\times t$. One also remarks that $U_n(t)$ in eq 21 is not monotonous.
 547 The function passes through a minimum at short times (small
 548 strains), as the phenomenological eq 20 is purely relaxational.
 549 For large enough strains, the growth rate becomes positive, and
 550 $U_n(t)$ grows exponentially. The growth starts when ϵ_{zz}
 551 corresponds to the buckling strain ($\epsilon_{zz} = \epsilon_{zz}^*(k)$) for which
 552 $F(\epsilon_{zz}(t), k) = 0$. The decreasing part of the curve prior to
 553 buckling is irrelevant, as thermal fluctuations are ignored in eq
 554 20.

555 Equation 20 has been solved numerically using a fourth order
 556 Runge–Kutta method starting from an arbitrary small value of
 557 $U_n(0)$. The value of Λ and $U_n(0)$ were determined by the

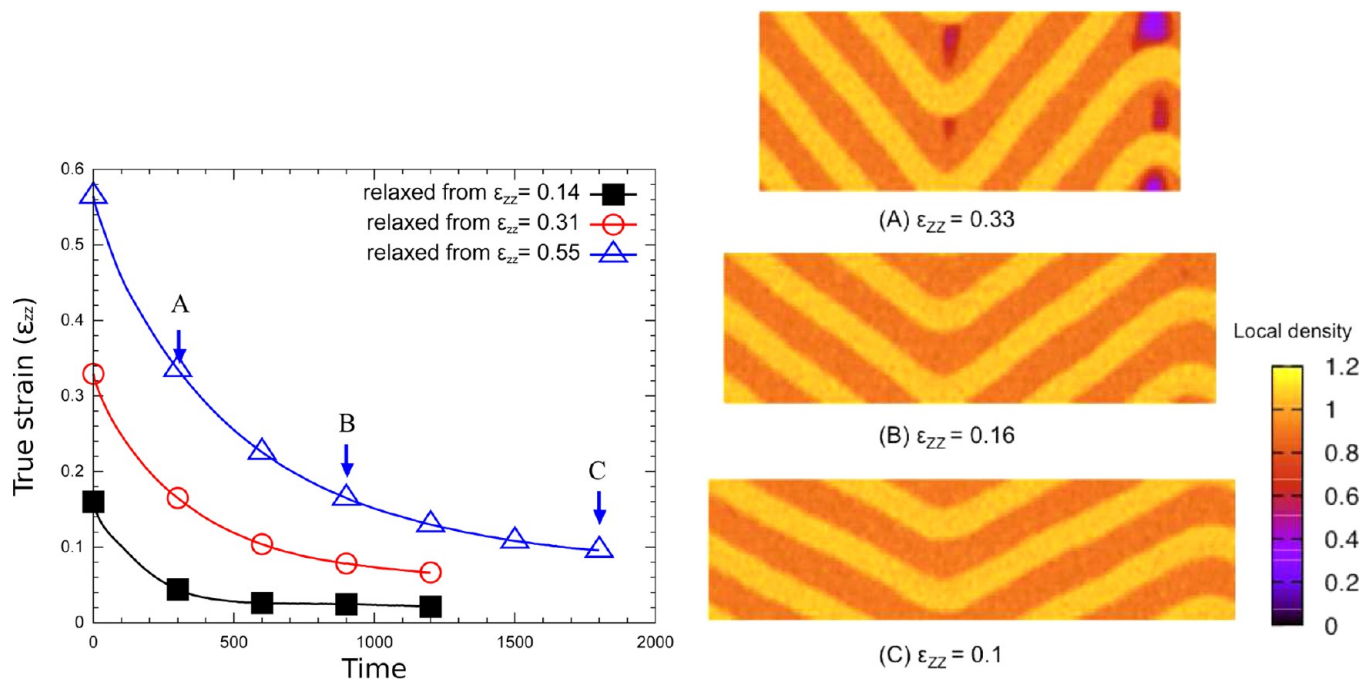


Figure 11. Left: relaxation of the strain in a system unloaded instantaneously after being deformed to the strains indicated in the figure. Right: snapshots of the relaxing configuration (density field) at the three states indicated by A, B, C in the left panel.

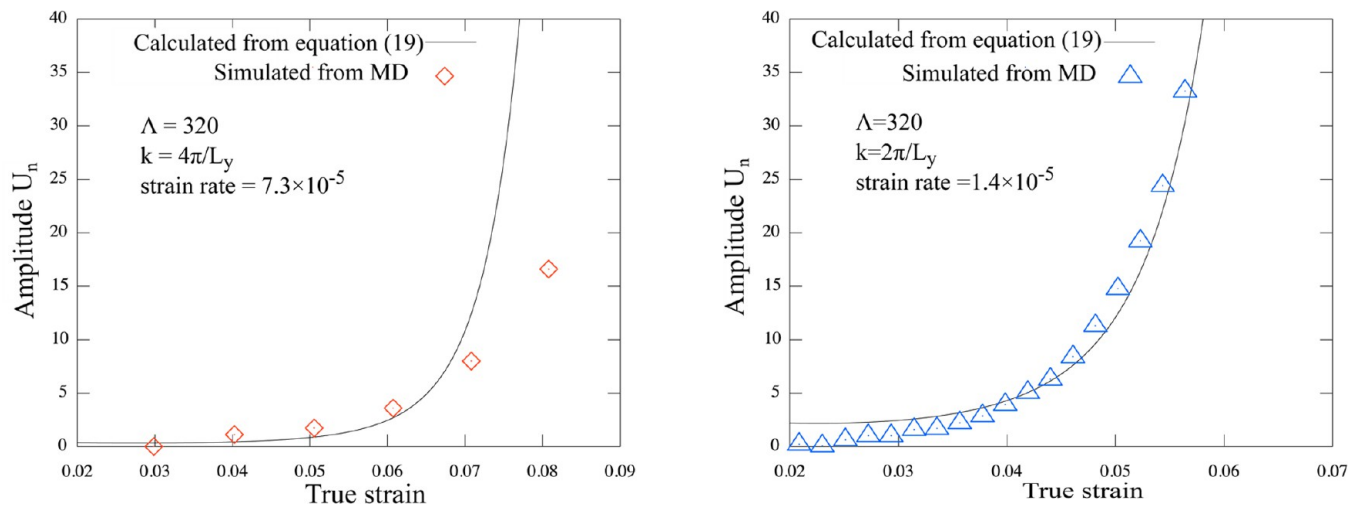


Figure 12. Comparison between the measured values of buckling amplitude (disconnected symbols) and the value calculated from eq 9 (full lines) for the largest sample $L_y = 787.2\sigma$. The left panel corresponds to fundamental mode $k = 2\pi/L_y$, observed at low strain rate, whereas the right panel corresponds to the second mode $k = 4\pi/L_y$ at high strain rate. The value of Λ taken here corresponds to the best fit of the measured amplitude.

560 solution that ensures the best fit of the buckling amplitude
 561 measured during the deformation of the largest sample S_{24} at
 562 low and high strain rate (see Figure 12). Note that the largest
 563 sample was chosen for the fit because the two buckling modes
 564 $2\pi/L_y$ and $4\pi/L_y$ can be clearly distinguished at two different
 565 strain rates. We find that the best fit is obtained for $\Lambda = 320$
 566 and the initial value of $U_n(0) = 0.03$. This initial value of the
 567 amplitude can be considered as corresponding to the level of
 568 heterogeneity of the initial sample, which serves to initiate the
 569 buckling.

570 **Results and Discussion.** Having fixed Λ and $U_n(0)$, eq 20
 571 has been solved for different values of wave vectors $2\pi/L_y$ and
 572 $4\pi/L_y$ at two different strain rates $\dot{\epsilon}_{zz} = 7.3 \times 10^{-5}$ and $\dot{\epsilon}_{zz} = 1.4$
 573 $\times 10^{-5}$. The results were plotted and compared in Figure 13.
 574 This figure shows that (i) the buckling strain increases as the

buckling wave vector increases, as expected; (ii) at the same
 575 strain rate, the second buckling mode is faster to develop,
 576 compared to the fundamental mode. Moreover the second
 577 mode growth intercepts the fundamental buckling growth at a
 578 certain strain (called below switching strain, ϵ_{sw}) for both strain
 579 rates. At this strain the second buckling mode can overtake the
 580 fundamental mode if the latter has not fully developed. For the
 581 low strain rate case, the fundamental buckling mode starts
 582 growing at a low strain, and is well developed when the strain
 583 reaches ϵ_{sw} , so that the system can not switch to higher buckling
 584 mode, and the fundamental mode is selected. In contrast, at
 585 high strain rate the first mode has grown to a small amplitude
 586 when the sample reaches ϵ_{sw} , so that the second mode can
 587 easily overwhelm the fundamental mode and the sample adopts
 588 a higher mode for buckling.
 589

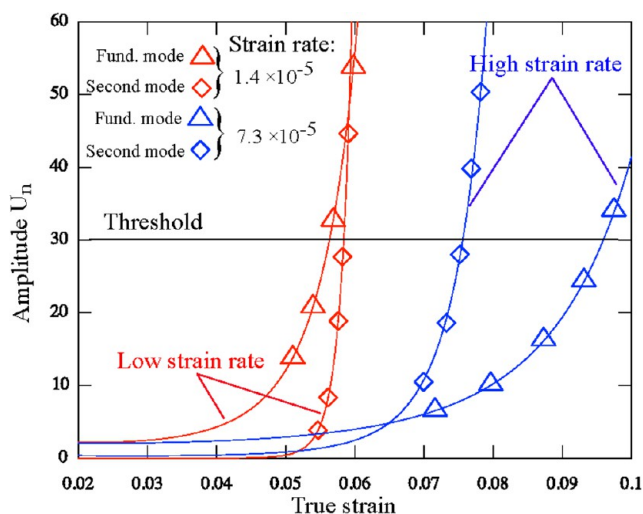


Figure 13. Comparison between the growth of the fundamental mode and of the second mode for the largest sample at two different strain rates. The higher mode develops faster than the lower mode even if the instability of the latter is triggered at first. The threshold is chosen so that it intersects first the fundamental mode at low strain rate, and the second mode at high strain rate.

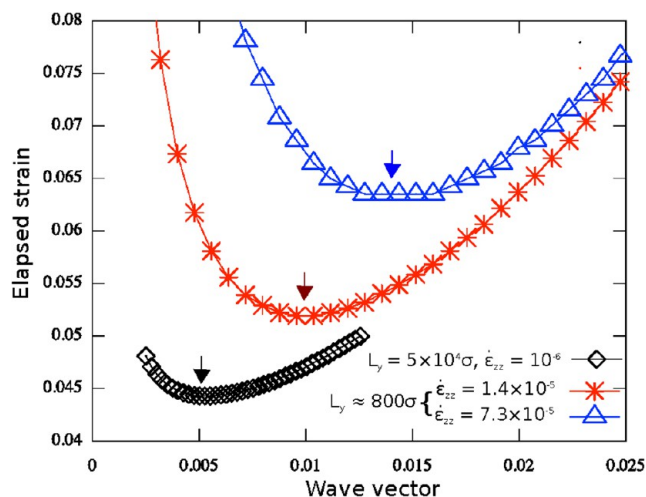


Figure 14. True strain elapsed from the beginning of the deformation to reach the threshold for different buckling wave vectors, according to the kinetic model: the minimum corresponds to the “winner mode”, that will be adopted by the sample. Several different system sizes and strain rates varying over 2 orders of magnitude are considered.

590 From the previous analysis, one can define a critical buckling
591 amplitude: as the amplitude threshold after which the selection
592 of the buckling mode is prohibited. This means that the buckling
593 mode that reaches this threshold at the first is the one that is
594 adopted by the sample to achieve the buckling. This mode is
595 called hereafter the “winner mode”. Quantitatively speaking the
596 “winner mode” of buckling is defined when the strain elapsed to
597 reach the critical amplitude is minimum.

598 The critical amplitude threshold can be determined
599 approximately from Figure 13. This threshold graphically
600 located in the middle of the interval delimited by the two
601 switching points (this term designates the switching from the
602 fundamental to the second mode only) for each strain rate
603 curves. For the rest of analysis, the amplitude threshold was
604 taken to be $U^* = 30\sigma$; at this value, the threshold crosses the
605 fundamental mode growth at first at a low deformation rate
606 while it crosses the second mode at first at a high deformation
607 rate.

608 Obviously, the procedure that consists in fixing the amplitude
609 threshold at which a mode will become predominant is
610 empirical. The actual mechanism for mode selection presumably
611 involves nonlinear interactions between modes, which are
612 not accounted for in the present description.

613 **Generalization.** In order to generalize the previous analysis,
614 let one consider a large sample that is deformed at an imposed
615 strain rate $\dot{\epsilon}_{zz}$. The choice of a large sample size leads to very
616 close values of wave vectors $2\pi/L_y \approx 4\pi/L_y \approx 6\pi/L_y \dots$. To
617 identify the mode that is likely to be selected, one has to
618 compute the growth of the amplitude for each mode, which was
619 done using the same parameter Λ as above. The strain needed
620 for the amplitude of a mode to reach the threshold U^* can then
621 be computed as a function of k . The result is plotted in Figure
622 14. The curve passes through a minimum that separates two
623 regimes: the decreasing portion of the curve that corresponds
624 to the fact that the development of buckling becomes faster as
625 the buckling wave vector increases. The second regime, after
626 the minimum, corresponds to the increase of the buckling
627 strain observed when the buckling wave vector increases. The

value of the minimum gives the wavevector that will be selected
at the strain rate under consideration. Besides the approx-
imation of using a wavevector independent threshold, this
prediction also ignores the nucleation of cavities observed at
extremely high strain rate and neglects any variation of Λ with
respect to the deformation rate.

VIII. CONCLUSION

In this paper, the mechanical response of triblock copolymer
models in the lamellar phase has been investigated by using a
coarse grained molecular dynamic simulation. Our MD samples
were built by radical like polymerization method, and alternate
glassy and rubbery lamellae. Uniaxial tensile tests were
performed in the direction normal to the layers. The resulting
constitutive laws are compared to the change of sample
morphology and microstructure.

Depending on the applied deformation rate, the samples
exhibit a variety of microscopic deformation mechanisms. At
relatively high strain rate, one observes (except for the shortest
samples) a buckling of the lamellae into a wavelength that does
not depend on the sample size. The buckling is accompanied by
the nucleation of cavities in the rubbery phase. Both events
were found to contribute to the drop stress at yield. At low
strain rate, all samples (including the shortest one) exhibit
buckling. The yield becomes correlated with the onset of the
lamellae buckling, and the cavitation is delayed. The undulation
wavelength is almost equal to the sample length in this case.
The buckling strain of each sample was calculated using the
elastic theory approach. The results were compared to the
values observed in the MD simulations. A strong deviation was
found at high strain rate; however, at low strain rate, the results
are consistent.

This behavior was rationalized by using a simplified model of
mode growth based on a viscous dynamics and on an elastic
driving force for the mode amplitudes. This model shows that
the higher mode of buckling is faster to develop compared to
the fundamental mode, although the latter is the first to become
unstable. When the strain rate increases, several modes come
into competition. The shortest wavelength that corresponds to
a larger driving force can take over and dominate the instability

666 pattern. In this case the strain for observing buckling can be
667 markedly larger than predicted by elastic theory.

668 We finally turn to a short discussion of the relevance of our
669 results to experimental situations. Our simulations use a coarse
670 grained model, which is not specific to any material, and is
671 defined in terms of typical energy, mass and size. Using an
672 energy scale of $1000K \times k_B$ and a length scale of 0.5 nm, which
673 are typical in the coarse-grained descriptions of standard
674 polymers, the corresponding stress unit is of order 100 MPa,
675 and the Young modulus of the glassy polymer is of the order of
676 1–10 GPa. The time scale that results from these choices of
677 units, if parameters appropriate for typical polymers are used,
678 lies in the picosecond time range. Therefore, the strain rates
679 achieved in simulations are of the order of $10^7 s^{-1}$ in real units,
680 extremely high compared to typical experimental rates. As is
681 often the case in simulation studies involving glassy materials,
682 the behavior observed in simulation studies must be under-
683 stood as being qualitatively, rather than quantitatively,
684 representative of the experimental reality. However, there are
685 several arguments that are indicative of the relevance of the
686 mechanism observed and modeled in this paper to
687 experimental situations. First of all, it is known from
688 experiments that plasticity is usually observed for strains of at
689 least 5%. For such values of the strain, the wavelength that are
690 energetically favorable within the elastic theory are quite small,
691 as can be seen from Figure 5, and typically in the 100 nm range.
692 The issue is then to understand, why such wavelengths are
693 selected within the experimentally slow deformation process, as
694 opposed to larger wavelengths that should be selected in a truly
695 quasistatic approach. Our molecular simulations and the
696 associated kinetic model are a good indicator here. Molecular
697 simulations indicate that the critical strain predicted by the
698 static elastic theory is observed for the lowest strain rates that
699 can be achieved in simulation, which are still very high
700 compared to experiments. These results are rationalized on the
701 basis of a kinetic model, and the extrapolation to lower strain
702 rates using the kinetic model indicates that the preferred
703 wavelength will be weakly sensitive to strain rate over a broad
704 range of values, with a selected wavelength that increases by
705 only a factor of 2 for a change of more than 1 order of
706 magnitude in the strain rate (see Figure 14). Unfortunately the
707 limitations of the model, which considers a strain rate
708 independent kinetic coefficient, does not allow us to extrapolate
709 reliably to experimental strain rates. Another qualitative
710 prediction that can be made on the basis of our analysis
711 concerns the temperature dependence of the chevron pattern;
712 as the kinetic coefficient Λ is expected to increase with
713 temperature ($1/\Lambda$ can be associated with a viscosity), the
714 threshold for instability will be reached earlier for larger
715 wavelength. Therefore, the wavelength is expected to increase
716 with increasing temperature as it does with decreasing strain
717 rate, in line with general time–temperature considerations.

718 ■ AUTHOR INFORMATION

719 Corresponding Author

720 *E-mail: (J.-L.B.) jean-louis.barrat@ujf-grenoble.fr..

721 Notes

722 The authors declare no competing financial interest.

723 ■ ACKNOWLEDGMENTS

724 Computational support was provided by the Federation
725 Lyonnaise de Calcul Haute Performance and GENCI/CINES

. Financial support from ANR Project Nanomeca is acknowl-
edged. J.-L.B. is supported by the Institut Universitaire de
France. Part of the simulations were carried out using the
LAMMPS molecular dynamics software (<http://lammps.sandia.gov>). The snapshots were visualized using VMD
software²⁴ (<http://www.ks.uiuc.edu/Research/vmd/>).

■ REFERENCES

- (1) Bates, F.; Fredrickson, G. *Phys. Today* **1999**, *52*, 32.
- (2) Michler, G.; Adhikari, R.; Henning, S. *J. Mater. Sci.* **2004**, *39*, 3281–3292.
- (3) Krumova, M.; Henning, S.; Michler, G. H. *Philos. Mag.* **2006**, *86*, 1689–1712.
- (4) Koo, M.; Wu, L.; Lim, L.; Mahanthappa, M.; Hillmyer, M.; Bates, F. *Macromolecules* **2005**, *38*, 6090–6098.
- (5) Hermel, T.; Hahn, S.; Chaffin, K.; Gerberich, W.; Bates, F. *Macromolecules* **2003**, *36*, 2190–2193.
- (6) Burnay, S.; Groves, G. J. *Mater. Sci.* **1977**, *12*, 1139–1142.
- (7) Bochl, G.; Owen, A. *Colloid Polym. Sci.* **1984**, *262*, 793–797.
- (8) Bartczak, Z.; Lezak, E. *Polymer* **2005**, *46*, 6050–6063.
- (9) Mohanraj, J.; Morawiec, J.; Pawlak, A.; Barton, D.; Galeski, A.; Ward, I. *Polymer* **2008**, *49*, 303–316.
- (10) Cohen, Y.; Albalak, R.; Dair, B. *Macromolecules* **2000**, *33*, 6502.
- (11) Mori, Y.; Lim, L.; Bates, F. *Macromolecules* **2003**, *36*, 9879–9888.
- (12) Mahanthappa, M.; Hillmyer, M.; Bates, F. *Macromolecules* **2008**, *41*, 1341–1351.
- (13) Phatak, A.; Lim, L.; Reaves, C.; Bates, F. *Macromolecules* **2006**, *39*, 6221–6228.
- (14) Honeker, T.; Christian, C.; L, E. *Chem. Mater.* **1996**, *8*, 1702–1714.
- (15) Diamant, J.; W, M. C.; S, S. D. *Polym. Eng. Sci.* **1988**, *28*, 207–220.
- (16) Adhikari, R.; Michler, G. *Prog. Polym. Sci.* **2004**, *29*, 949–986.
- (17) Cohen, Y. *Macromolecules* **2001**, *33*, 6502–6516.
- (18) Read, D. J.; Duckett, R.; Sweeny, J.; McLeish, T. J. *Phys. D: Appl. Phys.* **1999**, 2087–2099.
- (19) Makke, A.; Lame, O.; Perez, M.; Barrat, J.-L. *Macromolecules* **2012**, *45*, 8445–8452.
- (20) Makke, A.; Perez, M.; Lame, O.; Barrat, J. J. *Chem. Phys.* **2009**, *131*.
- (21) Makke, A.; Perez, M.; Lame, O.; Barrat, J. *Proc. Natl. Acad. Sci. U.S.A.* **2012**, *109* (3), 680–685.
- (22) Kremer, K.; Grest, G. J. *Chem. Phys.* **1990**, *92*, 5057–5086.
- (23) Perez, M.; Lame, O.; Leonforte, F.; Barrat, J. J. *Chem. Phys.* **2008**, *128*, 234904.
- (24) Humphrey, W.; Dalke, A.; Schulten, K. *J. Mol. Graphics* **1996**, *14*, 33–38.